A Complex Ray-Tracing Tool for High-Frequency Mean Field Flow-Interaction Effects in Jets

J. T. Stone[*] and R. H. Self[†]

Institute of Sound and Vibration Research, University of Southampton, Highfield, Southampton, SO17 1BJ, UK.

C. J. Howls[‡]

Mathematical Sciences, University of Southampton, Highfield, Southampton, SO17 1BJ, UK.

This paper presents a complex ray-tracing tool for the calculation of high-frequency Green's functions in 3D mean field jet flows. For a generic problem, the ray solution suffers from three main deficiencies: multiplicity of solutions, singularities at caustics, and the determining of complex solutions. The purpose of this paper is to generalize, combine and apply existing stationary media methods to moving media scenarios. Multiplicities are dealt with using an equivalent two-point boundary-value problem, whilst non-uniformities at caustics are corrected using diffraction catastrophes. Complex rays are found using a combination of imaginary perturbations, an assumption of caustic stability, and analytic continuation of the receiver curve. To demonstrate this method, the ray tool is compared against a high-frequency modal solution of Lilley's equation for an off-axis point source. This solution is representative of high-frequency source positions in real jets and is rich in caustic structures. A full utilization of the ray tool is shown to provide excellent results.

I.   Introduction

As industrial design continues to look at less conventional jet engine nozzles that produce typically asymmetric mean flows, there is now a need for completely 3D noise prediction schemes. To date, most prediction schemes have been based on extensions of the acoustic analogy given by Lighthill:[1,2] for instance Lilley[3] for a parallel shear flow, and more recently the generalized acoustic analogy due to Goldstein[4] for arbitrary flows. The acoustic analogy procedure starts from the nonlinear fluid dynamic equations assuming that one can decompose the field variables into the sum of mean and fluctuating parts for small disturbances. The equations are then linearized about a representative base flow retaining the non-linear terms as part of prescribed source term. Since the non-linear source term in the analogy is either known *a priori* or can be modelled statistically, the problem may be reduced to the determination of the mean-field Green's function.

It is well known that the Green's function for a generic moving media problem has no closed form solution and only in the cases of constant flow and parallel shear flow can one form a wave equation in one variable without recourse to perturbation methods. However, since the noise produced in many aeroacoustic problems is dominated by high-frequency sources, it is expedient to look for a form of solution that exploits the small wavelength nature of the acoustic field. Such a form is offered by geometrical acoustics, where a WKB (see for e.g. Brekhovskikh[5]) type series is formally introduced into the governing equations and an infinite system of simpler equations generated. The method of characteristics can then be used to solve the leading equations of phase and amplitude in terms of an initial value problem (IVP), the integral curves of which are known as rays.

Real ray theory as a method of computing high-frequency flow-interaction effects in jets is not new, having been used by Candel[6] for mean fields and Freund et al.[7] for turbulent fields. However, there is yet to be an efficient framework for dealing with a fully complexified ray problem in moving media that takes account of deficiencies that would be expected in a free-field scenario.

---

[*]PhD Student, ISVR, University of Southampton, UK, AIAA Student Member.
[†]Senior Lecturer, ISVR, University of Southampton, UK, AIAA Member.
[‡]Senior Lecturer, Mathematical Sciences, University of Southampton, UK.

American Institute of Aeronautics and Astronautics

In this paper we seek to provide a framework that takes account of these deficiencies, utilizing methods that exist in other branches of high-frequency theory. The deficiencies we are concerned with are the following: the arrival of multiple ray trajectories at a given receiver location, the determination and tracking of complex solutions, and the divergence of ray amplitudes at caustics.

The first two deficiencies are addressed in Section II. Defining the general problem as a point source solution to the linearized acoustic equations, we use the time-harmonic matched ray method due to Avila & Keller[8] and Durbin[9] to express a generic ray contribution to the field, recasting the resulting ray IVP as a nonlinear boundary value problem (BVP) that explicitly represents the receiver. The roots of the BVP correspond to rays that propagate to the desired receiver point and their determination is non-trivial. The simplest scheme for approximating these roots is through an equivalent functional iteration effected by Newton's method. If we traverse a receiver curve natural parameter continuation can then be used to generate a series of solution curves or branches. At caustics several of these curves will bifurcate generating a set of new, possibly complex, solution branches. This makes a caustic ideal for transitioning from real rays to complex rays, and one we take advantage of by introducing a simple complex continuation method that generates a nearly complete set of solutions.

In Section III we correct the divergences shown at caustics by employing a classification program known as catastrophe theory (Gilmore[10]). We determine all coalescing ray contributions at a caustic, thus allowing us to identify an appropriate uniform solution, known as a diffraction catastrophe, that remains bounded at the caustic. An expansion of the field locally using this method leads to an ordered asymptotic sequence in the diffraction catastrophe and its derivatives. In this paper we consider only cuspoid catastrophes, the simplest, and most familiar is the Airy function used by Ludwig[11] to describe the high-frequency field in the vicinity of a fold caustic.

The final part of this paper, presented in Section IV, is devoted to validating the ray tool. We consider an isothermal parallel shear flow whereby the governing acoustic equations can be manipulated into Lilley's equation. Using a high-frequency modal solution of Lilley's equation due to Wundrow & Khavaran[12] we show that the complex ray-tracing tool developed in Sections II and III can achieve excellent accuracy, particularly in the shadow zone known as the cone of silence. The authors believe that this is the first numerical realization of complex rays using ray trajectories for this flow regime.

II.   Theoretical basis.

A.   High-frequency ray solution.

As the starting point for our ray solution we consider the inviscid, inhomogeneous continuity and momentum equations linearized about a mean flow. For a time harmonic field proportional to $e^{-i\omega t}$ these are

$$-i\omega\rho' + \nabla \cdot (\bar{\boldsymbol{u}}\rho' + \boldsymbol{u}'\bar{\rho}) = \bar{\rho}q,$$

$$-i\omega\boldsymbol{u}' + \bar{\boldsymbol{u}} \cdot \nabla\boldsymbol{u}' + \boldsymbol{u}' \cdot \nabla\bar{\boldsymbol{u}} + \nabla\left(\bar{c}^2\rho'/\bar{\rho}\right) = \boldsymbol{f}/\bar{\rho}, \tag{1}$$

where ρ' and $\boldsymbol{u}'$ are the acoustic density and particle velocity; $\bar{\rho}$, $\bar{\boldsymbol{u}}$, and $\bar{c}$ are the density, velocity, and sound speed of the mean field; and ω is the frequency. The quantities q and $\boldsymbol{f}$ are externally applied volume sources that, for the construction of a Green's function, are replaced by an appropriate point source.

The high-frequency Green's function for the acoustic density in Eqs. (1) that we now derive is due to Durbin.[9] The full details can be found therein, however for the purposes of this paper it is expedient to outline the bare bones of the ray matching method.

The matching method consists of two parts, summarized in Figure 1: we derive a ray solution away from the point source (shown in red) in the outer region, so that we only deal with the homogeneous system of Eqs. (1); we then calculate the near source solution, or "inner" solution by introducing an inner variable that captures the rapid variation of the point source. Assuming the existence of a transition region where the two solutions overlap, the method of matched asymptotic expansions (see for e.g. Van Dyke[13]) assures a match.

1.   Near source solution.

In the vicinity of the point source the mean field quantities assume constant values (denoted by subscript s) so that all derivatives of these terms appearing in Eqs. (1) may be discarded. Close to the source it is

American Institute of Aeronautics and Astronautics

appropriate to use an inner variable $\boldsymbol{y} = k_0(\boldsymbol{x} - \boldsymbol{x}_s)$, where $\boldsymbol{x}_s$ is the source location, $k_0 = \omega/\bar{c}_\infty$ is the characteristic wavenumber of the field, and $\bar{c}_\infty$ is a reference sound speed[a].

An inner wave equation for ρ' is then formed to give,

$$(\rho'/a_s^2) + 2\mathrm{i}(\boldsymbol{M}_s \cdot \nabla_{\boldsymbol{y}}\rho'/a_s) + \nabla_{\boldsymbol{y}} \cdot \boldsymbol{T}_s \cdot \nabla_{\boldsymbol{y}}\rho' = -\delta(\boldsymbol{y})k_0, \tag{2}$$

where $a = \bar{c}/\bar{c}_\infty$ and $\boldsymbol{M} = \bar{\boldsymbol{u}}/\bar{c}$ are the dimensionless sound speed and local Mach number, respectively. The matrix $\boldsymbol{T}$ and its inverse are defined, using index notation and the kronicker delta δ_{ij}, as,

$$T_{ij} = \delta_{ij} - M_i M_j, \quad T_{ij}^{-1} = \delta_{ij} - M_i M_j/\beta^2, \quad \beta^2 = 1 - M_i M_i. \tag{3}$$

In the derivation of Eq. (2) the source distribution $\bar{\rho}_s/\bar{c}_s^2(\mathrm{i}\omega - \bar{\boldsymbol{u}}_s \cdot \nabla)q + \nabla(\boldsymbol{f}/\bar{c}_s^2)$ has been replaced by the scaled delta function $-\delta(\boldsymbol{y})k_0$ to form the Green's function for ρ'. Equation (2) is soluble in terms of Hankel functions under a suitable transformation so the inner solution according to Durbin[9] is,

$$\rho' \sim \mathrm{ie}^{\mathrm{i}\boldsymbol{y}\cdot\boldsymbol{M}_s}\mathrm{H}_{1/2}^{(1)}(\eta/\beta_s a_s)k_0/4\beta_s(2\pi\eta a_s\beta_s)^{1/2}, \quad \eta^2 = \boldsymbol{y} \cdot \boldsymbol{T}_s^{-1} \cdot \boldsymbol{y}. \tag{4}$$

2. Outer source solution

The outer ray solution is found by formally substituting the following asymptotic series for the acoustic density and particle velocity into the homogeneous system of Eqs. (1).

$$\rho' \sim \mathrm{e}^{\mathrm{i}k_0 S(\boldsymbol{x})} \sum_{n=0}^{\infty} \frac{A_n(\boldsymbol{x})}{(\mathrm{i}k_0)^n}, \quad \boldsymbol{u}' \sim \mathrm{e}^{\mathrm{i}k_0 S(\boldsymbol{x})} \sum_{n=0}^{\infty} \frac{\boldsymbol{A}_n(\boldsymbol{x})}{(\mathrm{i}k_0)^n}. \tag{5}$$

Equating all terms that are premultiplied by the same power of k_0 leads to an infinite system of recurrence relations in S, A_n, and $\boldsymbol{A}_n$.[5,6] The "asymptoticness" of the ray ansatz assures that for quantitative purposes we need only calculate the phase S and leading amplitude terms A_0 and $\boldsymbol{A}_0$.

The phase S satisfies the eikonal equation,

$$\frac{1}{2}(\nabla S \cdot \boldsymbol{T} \cdot \nabla S) + (\boldsymbol{M} \cdot \nabla S)/a - 1/2a^2 = 0, \tag{6}$$

which can be solved by introducing rays that are the characteristics of Eq. (6) (see for e.g. Bleistein[14]). The phase of the field may be determined by propagating rays $\boldsymbol{x}(\tau)$ from the source according to the initial value problem (IVP),

Figure 1. **Illustrating the matching procedure.** The inner region (blue) surrounding the point source (red) must have an overlap/transition region (orange) with the outer region.

$$\dot{x}_i = T_{ij}(\boldsymbol{x})p_j + \frac{M_i(\boldsymbol{x})}{a(\boldsymbol{x})}, \quad \dot{p}_i = -\frac{1}{2}p_j\frac{\partial T_{jk}(\boldsymbol{x})}{\partial x_i}p_k - p_j\frac{\partial}{\partial x_i}\left(\frac{M_j(\boldsymbol{x})}{a(\boldsymbol{x})}\right) + \frac{1}{2}\frac{\partial a^{-2}(\boldsymbol{x})}{\partial x_i},$$

$$\dot{S} = p_i\dot{x}_i, \tag{7}$$

where $\boldsymbol{p} = \nabla S$, and $\dot{} \equiv \mathrm{d}/\mathrm{d}\tau$. Only in the simplest cases (e.g. homogeneous media) can Eqs. (7) be solved analytically, so the standard procedure is to integrate, or "fire off", $\boldsymbol{x}(\tau)$ numerically.

Firing off a ray from a point source in 3D requires two angular parameters $\tilde{\mu} = \{\mu, \lambda\}$ along with one integration parameter τ. The initial firing normal $\tilde{\nu}_s = (\cos\mu, \sin\mu\cos\lambda, \sin\mu\sin\lambda)$ is chosen to be proportional to the ray group velocity $\dot{x}_i = \sigma_s\tilde{\nu}_s$, where the constant of proportionality σ is the ray speed defined by $\sigma = \sqrt{\dot{x}_i\dot{x}_i}$. Thus the IVP has initial conditions:

$$x_i(0) = x_{i_s}, \quad p_i(0) = T_{s_{ij}}^{-1}\left(\sigma_s\tilde{\nu}_{s_j} - \frac{M_{s_j}}{a_s}\right), \quad \sigma_s^{-2} = \left(\tilde{\nu}_{s_i}T_{s_{ij}}^{-1}\tilde{\nu}_{s_j}\right)a_s^2\beta_s^2, \quad S(0) = 0. \tag{8}$$

---

[a]We take this as the sound speed in a quiescent medium. $\bar{c}_\infty = 340\,\mathrm{m/s}$ when required.

3. Amplitude, amplitude match & derived ray equations.

The amplitude term of interest $A_0(\boldsymbol{x})$ for calculating the acoustic density can be shown to satisfy a conservation law along the rays,[5]

$$\nabla \cdot \left(\frac{A_0^2 \dot{\boldsymbol{x}}}{\bar{\rho} \left[\frac{1}{a} - \boldsymbol{M} \cdot \boldsymbol{p} \right]^2} \right) = 0, \quad \text{so that,} \quad \frac{A_0^2 \sigma J}{\bar{\rho} \left[\frac{1}{a} - \boldsymbol{M} \cdot \boldsymbol{p} \right]^2} = \text{const.}, \tag{9}$$

using the standard argument of a ray tube (Whitham[15]), and using the Jacobian, J, the determinant of the Jacobian matrix,

$$J_{\text{mat}} = \begin{pmatrix} \partial x_1/\partial \mu & \partial x_2/\partial \mu & \partial x_3/\partial \mu \\ \partial x_1/\partial \lambda & \partial x_2/\partial \lambda & \partial x_3/\partial \lambda \\ \partial x_1/\partial \tau & \partial x_2/\partial \tau & \partial x_3/\partial \tau \end{pmatrix}. \tag{10}$$

The constant in Eq. (9) is then found using the matching technique of Ref. 13 i.e. taking the limit $|\boldsymbol{y}| \to \infty$ in Eq. (4) and the limit $\boldsymbol{x} \to \boldsymbol{x}_s$ in leading term for density in Eq. (5) (using A_0 in Eq. (9)), and then equating in the transition zone shown in Figure 1. The constant is given as,[9]

$$\text{const.} = \sigma_s^3 a_s^2 \sin \mu / 4 (2\pi)^2 \bar{\rho}_s \left[\frac{1}{a_s} - \boldsymbol{M}_s \cdot \boldsymbol{p}_s \right]^2. \tag{11}$$

The expression for a generic ray contribution is then,

$$\rho' = A_0 e^{ik_0 S} = \left(\frac{\frac{1}{a} - \boldsymbol{M} \cdot \boldsymbol{p}}{\frac{1}{a_s} - \boldsymbol{M}_s \cdot \boldsymbol{p}_s} \right) \left(\frac{\bar{\rho} \sin \mu \, a_s^2 \sigma_s^3}{\bar{\rho}_s \sigma J} \right)^{1/2} \frac{e^{ik_0 S}}{4\pi}. \tag{12}$$

The only difficulty with calculating this expression now is the Jacobian appearing in Eq. (10). Here we use the derived ray equation (DRE) method due to Hayes.[16] Although, this method has been used previously by Candel,[6] the ray integration parameter and initial conditions (firing proportional to group velocity rather than $\boldsymbol{p}$) used here leads to both differences in the form of the DREs and in the numerical calculations.

The DRE method is simple: differentiate (using a partial derivative) the ray equations for x_i and p_i in Eq. (7) w.r.t the firing parameters to produce o.d.es for the elements $\partial x_i/\partial \tilde{\mu}$ in the Jacobian. There is no extra effort required to produce the elements $\partial \boldsymbol{x}/\partial \tau$ as these are interpreted as ordinary derivatives along the ray, and are calculated using $\dot{x}_i$ in Eq. (7).

Differentiating w.r.t the parameters $\tilde{\mu}$ leads to the following coupled o.d.es,

$$\frac{dy_{ik}}{d\tau} = \left[(\partial_n T_{ij}) \, p_j + \partial_n \left(\frac{M_i}{a} \right) \right] y_{nk} + T_{ij} z_{jk},$$

$$\frac{dz_{ik}}{d\tau} = \left[-\frac{1}{2} p_j \left(\partial_n \partial_i T_{jl} \right) p_l - p_j \partial_n \partial_i \left(\frac{M_j}{a} \right) + \frac{1}{2} \partial_n \partial_i \left(a^{-2} \right) \right] y_{nk} + \left[- (\partial_i T_{jl}) \, p_l - \partial_i \left(\frac{M_j}{a} \right) \right] z_{jk}. \tag{13}$$

where the $y_{ik} = \partial x_i/\partial \tilde{\mu}_k$ are the geodesic elements, and $z_{ik} = \partial p_i/\partial \tilde{\mu}_k$ the conjugate elements. The initial conditions for Eqs. (13) are derived by taking the same partial derivatives w.r.t the initial conditions in Eq. (8),

$$y_{ij}(0) = 0, \quad \forall i, j. \tag{14}$$

$$z_{ik}(0) = \frac{\partial \sigma_s}{\partial \tilde{\mu}_k} T_{s_{ij}}^{-1} \tilde{\nu}_{s_j} + \sigma_s T_{s_{ij}}^{-1} \frac{\partial \tilde{\nu}_{s_j}}{\partial \tilde{\mu}_k}, \quad \text{with,} \quad \frac{\partial \sigma_s}{\partial \tilde{\mu}_k} = -\sigma_s^3 a_s^2 \left(M_{s_n} \tilde{\nu}_{s_n} \right) \left(M_{s_j} \frac{\partial \tilde{\nu}_{s_j}}{\partial \tilde{\mu}_k} \right),$$

$$\text{so that,} \quad z_{ik}(0) = \sigma_s^3 a_s^2 \left(M_{s_n} \frac{\partial \tilde{\nu}_{s_n}}{\partial \tilde{\mu}_k} \right) \left(M_{s_i} - \left(M_{s_n} \tilde{\nu}_{s_n} \right) \tilde{\nu}_{s_i} \right) + \sigma_s \frac{\partial \tilde{\nu}_{s_i}}{\partial \tilde{\mu}_k}, \tag{15}$$

These equations form an extended IVP along with the ray IVP in Eqs. (7) and can be integrated numerically in the same way.

4. Complex Integration.

When we deal with complex rays we must allow every quantity we have dealt with so far to be complex. We have chosen dot products and square roots in the ray and derived ray equations so that it is straightforward to generalize these quantities to complex variables. Complex ray-tracing may proceed by directly integrating Eqs. (7) and (13) using a complex step as in Egorchenkov & Kravtsov,[17] however it is not so straightforward to generalize this method to arbitrary complex paths in practice. Instead we prefer to split the equations into their real and imaginary parts using a real parameterization of the complex path.

According to Eqs. (7) and (13) a generic ray quantity χ_i is propagated along a ray via the first order o.d.e,

$$\frac{\mathrm{d}\chi_i}{\mathrm{d}\tau} = \boldsymbol{f}(\chi_i, \boldsymbol{\chi}, \tau), \quad \text{with initial condition,} \quad \chi_i(0) = \chi_{i_s}, \tag{16}$$

where $\boldsymbol{\chi}$ represents all other dependent ray quantities that may appear in the l.h.s of Eqs. (7) and (13). Identifying that whenever $\tau \in \mathbb{C}$ we may use a real monotonically increasing variable $s_\tau = [0, 1]$, to represent the path as,

$$\tau = f_1(s_\tau) + \mathrm{i}f_2(s_\tau), \tag{17}$$

where $f_1, f_2 \in \mathbb{R}$. The variable χ_i is then split into real and imaginary parts i.e. $\chi_i = \chi_{i_\mathrm{Re}} + \mathrm{i}\chi_{i_\mathrm{Re}}$ so that coupled with Eq. (17), Eq. (16) may be expressed as the real o.d.e system,

$$\frac{\mathrm{d}\chi_{i_\mathrm{Re}}}{\mathrm{d}s_\tau} = f_1'(s_\tau)\Re(\boldsymbol{f}(\chi_i, \boldsymbol{\chi}, s_\tau)) - f_2'(s_\tau)\Im(\boldsymbol{f}(\chi_i, \boldsymbol{\chi}, s_\tau)), \quad \chi_{i_\mathrm{Re}}(0) = \Re(\chi_{i_s}),$$

$$\frac{\mathrm{d}\chi_{i_\mathrm{Im}}}{\mathrm{d}s_\tau} = f_2'(s_\tau)\Re(\boldsymbol{f}(\chi_i, \boldsymbol{\chi}, s_\tau)) + f_1'(s_\tau)\Im(\boldsymbol{f}(\chi_i, \boldsymbol{\chi}, s_\tau)), \quad \chi_{i_\mathrm{Im}}(0) = \Im(\chi_{i_s}), \tag{18}$$

where a prime denotes differentiation w.r.t s_τ. The only equation that does not have this form is the complex phase S, since the $\mathrm{d}\tau/\mathrm{d}s_\tau$ term cancels out in the last of Eqs. (7). The complex phase equation can be expressed as,

$$\frac{\mathrm{d}S_\mathrm{Re}}{\mathrm{d}s_\tau} = \Re(\boldsymbol{f}(S, \boldsymbol{\chi}, s_\tau)), \quad S_\mathrm{Re}(0) = 0,$$

$$\frac{\mathrm{d}S_\mathrm{Im}}{\mathrm{d}s_\tau} = \Im(\boldsymbol{f}(S, \boldsymbol{\chi}, s_\tau)), \quad S_\mathrm{Im}(0) = 0. \tag{19}$$

In this paper we will use the simplest parameterization possible i.e. a straight line between $\tau = 0$ and $\tau = \tau_R$, so that $f_{1,2}'$ are constant. It is, however, possible to integrate along any piecewise smooth path joining the integration endpoints given that there no singularities obstructing path deformation.

B. Two-point boundary problem and continuation methods.

1. Conversion to a boundary value problem (BVP).

As it remains the ray problem is a function of the ray parameters $\boldsymbol{s} = \{\tilde{\boldsymbol{\mu}}, \tau_R\}$ and not of the receiver coordinates $\boldsymbol{x}_R$. In general the relationship between these two is nontrivial. In order to represent the receiver explicitly we define the following function as in Sambridge & Kennett,[18]

$$\boldsymbol{F}(\boldsymbol{x}_R, \boldsymbol{s}) \equiv \boldsymbol{x}(\tau) - \boldsymbol{x}_R, \tag{20}$$

so that rays arriving at the receiver point satisfy $\boldsymbol{F} = \boldsymbol{0}$. We can solve Eq. (20) in terms of the ray parameters $\boldsymbol{s}$ by forming an iterative system of equations equivalent to it (see e.g. Keller[19]). The most effective procedure is a multidimensional Newton method applied to Eq. (20),

$$\boldsymbol{s}^{(k+1)} = \boldsymbol{s}^{(k)} - D\boldsymbol{F}^{-1}(\boldsymbol{s}^{(k)}; \boldsymbol{x}_R)\boldsymbol{F}(\boldsymbol{s}^{(k)}; \boldsymbol{x}_R), \tag{21}$$

where $D\boldsymbol{F}$ is the transpose of the Jacobian matrix Eq. (10), and k is an iteration counter. Utilization of Eq. (21) starts by firing a distribution of real test rays $\boldsymbol{s}^{(0)}$ for a receiver point and iterating the system until convergence, discarding all non-unique $\boldsymbol{s}$'s. Convergence is determined when user defined tolerances are met $|x_{i_R} - x_i(\tau_R)| < x_{i_{Tol}}$ such that $\boldsymbol{F} \approx \boldsymbol{0}$. It is preferable to start with real rays in this way because the domains of convergence of Eq. (21) for complex rays means an inaccurate guess will quickly lead to divergence. Complex solutions can be found using the methods discussed below.

2. Continuation at caustics.

For most calculations we are not just interested in the solution at just one point, but along a receiver curve generated by some monotonic scalar parameter within $\boldsymbol{x}_R$, α say. The simplest method of obtaining solutions is by using a natural parameter continuation whereby the solutions at $\boldsymbol{x}_R(\alpha)$ are used as the starting values for Eq. (21) at a nearby point $\boldsymbol{x}_R(\alpha + \delta\alpha) = \boldsymbol{x}_R + \delta\boldsymbol{x}_R$. Whenever $\det(D\boldsymbol{F}) \neq 0$ the implicit function theorem guarantees that a sequence of smooth curves $\boldsymbol{\Gamma_s}(\alpha)$ are generated in all ray parameters, $\boldsymbol{s}$, for each unique ray solution.[18] However, when $\det(D\boldsymbol{F}) = 0$ (i.e. $J = 0$) the receiver curve hits a caustic and several of the paths $\boldsymbol{\Gamma_s}$ will coalesce and then bifurcate upon increase of α. The coalescence of the bifurcation paths corresponds to the tangency of the ray trajectories (pertaining to the coalescing $\boldsymbol{s}$) of Eq. (7).

At a caustic Eq. (21) ceases to be effective for tracking all solutions that coalesce. Rather than recourse to elements of bifurcation theory to provide the local curve tangents at the bifurcation, we use a complex continuation method. The main advantage here is that the bifurcation formulae, which become increasingly complicated with increasing numbers of coalescing rays, may be avoided. We proceed by identifying all rays satisfying Eq. (20) that coalesce at the caustic point α_C in α-space. It is assumed that the caustic appears as a point in α-space, i.e $\boldsymbol{x}_R$ doesn't cut a caustic surface tangentially, and that other caustics aren't densely packed so that coalescences of bifurcation curves have some finite separation in α.

Starting at a point α_1 near the caustic, each coalescing ray solution can be analytically continued to the other side of the caustic α_2 by taking a path in complex α-space around α_C, so that $\boldsymbol{x}_R \in \mathbb{C}$ in Eq. (20). An example of two such paths is shown in Figure 2. The most straightforward paths are half-loops such as Path 1 and Path 2, although the exact path is arbitrary given sufficient distance from α_C.

The continuation method has the further advantage in that returning to the starting point α_1 (e.g Path 1 followed by the reverse of Path 2 in Figure 2) we may have passed smoothly onto another branch of the ray solution that wasn't picked up in the initial searches. In fact if a new solution is recorded then this branch should be continued around the caustic multiple times to generate the maximum number of new ray solutions at both α_1 and α_2. Doing so increases our chances of providing the appropriate local form to correct divergence at a caustic (see Section III), since this relies upon identifying all coalescing ray contributions at α_C.

Figure 2. Continuation of rays from α_1 around the caustic α_C to α_2. Where $\alpha_2 < \alpha_C < \alpha_1$.

Armed with this continuation method we can now recommend that complex rays are picked up using the continuation method whenever $\boldsymbol{x}_R$ encounters a caustic. The natural parameter continuation for rays looping around the caustic is much smoother than a bifurcation analysis across the caustic and thus proves suitable for connecting to complex branches where only a small sign-independent imaginary perturbation is required when leaving α_1.

As a final note in this section it is worth mentioning for consistency with the next section that in postulating the continuation method we have assumed implicitly that the caustics encountered are structurally stable (see for e.g. Berry & Upstill[20]). This means that each coalescing ray solution is behaving locally as the root of a polynomial and so smoothly continuing α means that we are effectively continuing the roots of this polynomial. This also ties in with another property of structural stability known as the conservation rays. Put simply this means that whenever a caustic is crossed the number of bifurcation paths, or roots of the polynomial, leading into the caustic must equal those coming out, even if they are complex. Complex bifurcation curves, if they exist, must then have a conjugate path so that the disappearance of real ray solutions across the caustic will always be in multiples of 2. When such complex cases arise we will always neglect exponentially growing rays pertaining to the conjugate branch in favor of exponentially decaying rays, on physical grounds. On this basis each of the N unique and physical ray contributions arriving at $\boldsymbol{x}_R$ may be summed as,

$$\rho' \sim \sum_{n=1}^{N} A_0^{(n)} \mathrm{e}^{\mathrm{i}k_0 S^{(n)}},\qquad(22)$$

where any phase discontinuities that arise due to propagation through caustics are implicit in the amplitudes $A_0^{(n)}$. For real rays these discontinuities must equal $-\pi/2$[20] so that numerical codes calculating Eq. (22) must have the correct square-root chosen in Eq. (12).
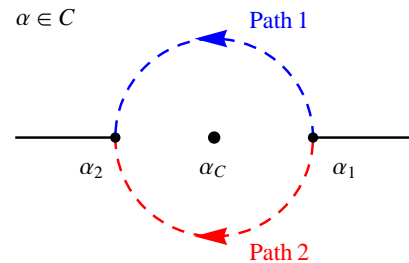
III.   Uniform solutions and catastrophe theory.

In the previous section we took advantage of caustics for continuing rays, finding new branches, and perhaps most importantly as a means for tracking complex rays. The downside is that coalescing rays fail on caustics completely by predicting unphysical intensity divergences. Not only do these rays fail at the caustic, but they diverge from the true field in a region around the caustic of $O(k_0^{-\gamma})$, where $\gamma > 0$ is a constant dependent on the type of caustic. Even though this region shrinks as $k_0 \to \infty$ it is still necessary to provide a correction at a caustic point. There are multiple ways of supplying uniformity at caustic, a good example being Maslov theory.[21] Here we choose to employ elements of catastrophe theory.[10]

Catastrophe theory allows us to replace coalescing ray contributions by a finite set of so-called diffraction catastrophes. These are local forms that remain uniform at caustic, but still exploit the $k_0 \to \infty$ properties of the acoustic field. They also exhibit an important mathematical property, and one we have already exploited, known as structural stability that requires the caustic to persist under perturbations of the initial field conditions (e.g. perturbations to the source position). There are two sets of stable caustics: the cuspoids and the umbilics;[20] in the following uniform derivation, analysis is restricted to the former.

In order to express the field in terms of diffraction catastrophes a hypothetical Kirchhoff integral, I, is postulated for the coalescing contributions. Away from the caustic, I, has the same asymptotic value as the ray contributions it represents. Using this theoretical device to represent $K + 1$ rays coalescing at the *same* caustic, Eq. (22) is rewritten as,

$$\rho' \sim \underbrace{\left(\frac{k_0}{2\pi i}\right)^{1/2} \int_{\mathscr{D}} a(\zeta; \boldsymbol{x}) e^{i k_0 \Phi(\zeta; \boldsymbol{x})} \, d\zeta}_{=I} + \underbrace{\sum_{n=n_K+1}^{N} A_0^{(n)} e^{i k_0 S^{(n)}}}_{\text{Rays not involved in caustic.}} \quad , \quad \mathscr{D} \in \mathbb{R}, \tag{23}$$

where $a(\zeta; \boldsymbol{x})$ is a slowly varying amplitude term, $\Phi(\zeta; \boldsymbol{x})$ is a generating function, and $n_K \le K + 1$ is the number of rays from Eq. (22) that are involved in the caustic. The great advantage of catastrophe theory is that we can write down this form without knowing the precise details of the system, only the local behavior matters, which is particularly useful since the most generic flow regimes don't allow us to write down a closed form integral for the acoustic field in the first place. It should be noted that Eq. (23) is easily generalizable to multiple groups of rays coalescing at different caustics.

Before the integral I in Eq. (23) is written in a form more convenient for our use, we define the cuspoids and diffraction catastrophes upon which the method is based. The cuspoids $\Psi_K(\boldsymbol{\xi})$ are defined as the following,

$$\Psi_K(\boldsymbol{\xi}) = \int_{-\infty}^{\infty} e^{i \psi_K(t; \boldsymbol{\xi})} \, dt, \quad \text{where}, \quad \psi_K = t^{K+2} + \sum_{m=1}^{K} \xi_m t^m, \tag{24}$$

and $\boldsymbol{\xi} = \{\xi_1, \xi_2, ..., \xi_K\}$ are control variables. The diffraction catastrophes $\tilde{\Psi}_K(\boldsymbol{\xi}; k_0)$ are then given by,

$$\tilde{\Psi}_K(\boldsymbol{\xi}; k_0) = \int_{-\infty}^{\infty} e^{i k_0 \psi_K(t; \boldsymbol{\xi})} \, dt = k_0^{-\frac{1}{K+2}} \Psi_K(\tilde{\boldsymbol{\xi}}), \quad \tilde{\boldsymbol{\xi}} = \{\xi_m k_0^{1 - \frac{m}{K+2}}\}. \tag{25}$$

The cuspoids form a hierarchy of functions in K different to the familiar functions of analysis. The cuspoid Ψ_1 is perhaps the most familiar as it is related to the Airy function via scalings i.e. $\Psi_1(\xi_1) = (2\pi/3^{1/3}) \text{Ai}(\xi_1/3^{1/3})$ and has been used previously by Ludwig[11] to describe the field at a fold caustic.

Aside from Ψ_1, a cuspoid we will make use of later in the paper is Ψ_2 which defines the Pearcey function $P(\xi_1, \xi_2) = \Psi_2(\xi_1, \xi_2)$.[22] As an example of the highly-oscilltory nature of the $\tilde{\Psi}_K$'s and Ψ_K's, Figure 3 shows the Airy function and its derivative along with $|\tilde{\Psi}_2(\boldsymbol{\xi})|$ in terms of the Pearcey function, and the modulus of the Pearcey function and its ξ_2 derivative on the line $\xi_1 = 0$.

Now we have defined the diffraction catastrophes - the essential building blocks of the method - we then use a generalization of Bleistein's technique[23,24] to expand the integral I in terms of $\Psi_K(\tilde{\boldsymbol{\xi}}; k_0)$ and its derivatives. We map from the ζ-plane to the t-plane using,

$$\Phi(\zeta; \boldsymbol{x}) = \psi_K(t; \boldsymbol{\xi}) + A, \quad A = \text{constant}, \tag{26}$$

and expand the amplitude function as,

$$a(\boldsymbol{x}) \frac{d\zeta}{dt} = \sum_{k=0}^{K} c_{k,0}(\boldsymbol{x}) t^k + \frac{d\psi_K}{dt} H_0(t; \boldsymbol{x}), \quad H_0 \in \mathscr{C}^{\infty}, \tag{27}$$
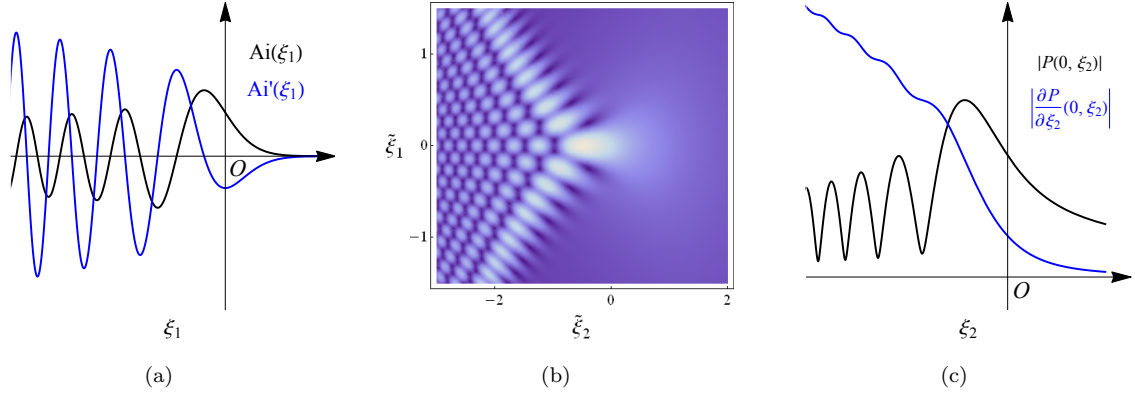
Figure 3. Example of functions found in uniform asymptotics. **Figure 3(a)** shows the Airy function and its first derivative; **Figure 3(b)** shows the amplitude of $|\tilde{\Psi}_2(\boldsymbol{\xi};k_0)| = \left|k_0^{-1/4}P(\tilde{\xi}_1,\tilde{\xi}_2)\right|$ (a value of $k_0 = 20$ is used); **Figure 3(c)** shows $|P(0,\xi_2)|$ and $|\partial P(0,\xi_2)/\partial \xi_2|$.

where $\mathrm{d}\zeta/\mathrm{d}t$ is the Jacobian of the mapping Eq. (26). Substitution of Eqs. (26) and (27) into I leads to the following,

$$I \sim (k_0/2\pi\mathrm{i})^{1/2}\,\mathrm{e}^{\mathrm{i}k_0 A}\left[k_0^{-\frac{1}{K+2}}\left(c_{0,0} + \sum_{n=1}^{K}\frac{c_{k,0}}{\mathrm{i}k_0}\frac{\partial}{\partial \xi_k}\right)\Psi_K(\tilde{\boldsymbol{\xi}}) - \frac{1}{\mathrm{i}k_0}\underbrace{\int_{\mathscr{D}}\frac{\mathrm{d}H_0}{\mathrm{d}t}\mathrm{e}^{\mathrm{i}_0 k_0 \psi_K}\mathrm{d}t}_{R_0}\right]. \tag{28}$$

The first terms in Eq. (28) contain Ψ_K and a finite number of its derivatives, and represent the beginnings of an ordered asymptotic sequence; the second term R_0 is a remainder term of $O(1)$. To generate the full asymptotic sequence we define the following $\mathscr{C}^\infty$ smooth functions,

$$\mathrm{d}H_m(t;\boldsymbol{x})/\mathrm{d}t = \sum_{k=0}^{K}c_{k,m+1}(\boldsymbol{x})t^k + (\mathrm{d}\psi_K/\mathrm{d}t)H_{m+1}(t;\boldsymbol{x}), \quad m \geq 0, \tag{29}$$

which, applied to the remainder integral R_0 and subsequent remainder integrals R_m,

$$R_m = \int_{\mathscr{D}}\frac{\mathrm{d}H_m}{\mathrm{d}t}\mathrm{e}^{\mathrm{i}k_0\psi_K}\,\mathrm{d}t, \tag{30}$$

leads to the full ordered asymptotic expansion for the Kirchhoff integral,

$$I \sim (k_0/2\pi\mathrm{i})^{1/2}\mathrm{e}^{\mathrm{i}k_0 A}\left[\sum_{m=0}^{\infty}\mathrm{e}^{\mathrm{i}m\pi/2}k_0^{-(m+\frac{1}{K+2})}\left(c_{0,m} + \sum_{k=1}^{K}c_{k,m}\mathrm{e}^{-\mathrm{i}\pi/2}k_0^{-k/(K+2)}\frac{\partial}{\partial \tilde{\xi}_k}\right)\Psi_K(\tilde{\xi})\right]. \tag{31}$$

For future reference it is worth noting that the ordered asymptotic sequence exhibited here allows us to consider only the $m = 0$ layer for future computations.

Clearly (given we can calculate the Ψ_K's and their first K derivs.) a uniform calculation of the field requires only the calculation of the coefficients $c_{k,m}$ and variables $\{\boldsymbol{\xi}, A\}$. In order to make tangible evaluations of these variables we can compare the Kirchhoff integral with the coalescing ray contributions off-caustic.

Expanding I in Eq. (23) (post t-plane mapping) using the saddle-point method[23] about *all* the $K+1$ saddles we then equate these contributions with the n_K coalescing contributions from Eq. (22), in addition to those rays that coalesce but are excluded on physical grounds. Though the correspondence between the saddles and the rays is not yet fixed, symbolically we have,

$$\left(a(t_n^\star)\frac{\mathrm{d}\zeta}{\mathrm{d}t}\bigg|_{t_n^\star}\right)\left(\frac{\mathrm{d}^2\psi_K}{\mathrm{d}t^2}\bigg|_{t_n^\star}\right)^{-1/2}\mathrm{e}^{\mathrm{i}k_0(\psi_K(t_n^\star)+A)} = A_0^{(n)}\mathrm{e}^{\mathrm{i}k_0 S^{(n)}}, \tag{32}$$

American Institute of Aeronautics and Astronautics

from which we deduce that,

$$a(t_n^\star) \left. \frac{\mathrm{d}\zeta}{\mathrm{d}t} \right|_{t_n^\star} = \left(\frac{\mathrm{d}^2\psi_K}{\mathrm{d}t^2} \right)^{1/2} A_0^{(n)}, \quad \text{and,} \quad \psi_K(t_n^\star) + A = S^{(n)},$$ (33)

where $t_n^\star$ is one of $K+1$ saddles such that $\mathrm{d}\psi_K(t_n^\star)/\mathrm{d}t = 0$ (referred to henceforth as the saddlepoint condition). It is the existence of this correspondence near the caustic that was used as motivation for the continuation method in Section II.B.2. The rays are behaving as the roots $t_n^\star$ of an order $K+1$ polynomial[b], thus our complex continuation method corresponds to varying these roots smoothly as functions of $\boldsymbol{\xi}$, which are in turn functions of $\boldsymbol{x}$ (see below).

We note that a saddle point comparison such as this seemingly remains valid only well away from the caustic. At a caustic saddles $t_n^\star$ coalesce so that $\mathrm{d}^2\psi_K(t_n^\star)/\mathrm{d}t^2 = 0$, and the corresponding rays have a singularity as J vanishes in Eq. (12). So then it may seem paradoxical, but in order to calculate the uniform expansions where they are required the most, we must rely on ray-tracing data and saddle point expansions in regions where they are known to fail (or least begin to diverge). In particular, the numerics must cope with the integrable singularity that occurs when,

$$\left(\left. \frac{\mathrm{d}^2\psi_K}{\mathrm{d}t^2} \right|_{t_n^\star} \right)^{1/2} / \left(J^{(n)} \right)^{1/2}, \quad \text{as} \quad \left. \frac{\mathrm{d}^2\psi_K}{\mathrm{d}t^2} \right|_{t_n^\star}, \, J^{(n)} \to 0,$$ (34)

at a caustic (using the expression for A_0 in Eq. (12)) so that Eq. (32) remains meaningful. By this we mean that $a(\zeta(t))$ contains no singularities and that the Jacobian of the map $\mathrm{d}\zeta/\mathrm{d}t$ is conformal. It is worth mentioning that if we had a closed form integral expression for the field, the integrable singularity would be tackled using a limiting device such as l'Hospital's rule (see for e.g. Bleistein & Handelsman[23]).

Returning to Eq. (33), we can fix the correspondence between saddles and rays by determining the variables $\{\boldsymbol{\xi}, A\}$, which was incidentally, our original goal. Unfortunately, as K increases so does the degree of difficulty in inverting these equations. In fact only for $K = 1, 2$[c] is there a closed form solution to this mapping, so we resort to the iterative method proposed by Connors & Curtis[25] to compute $\{\boldsymbol{\xi}, A\}$ and the $m = 0$ layer of coefficients $\{c_{k,0}\}$. This consists of making an initial guess $\{\boldsymbol{\xi}_i, A_i\} \in \mathbb{R}$[d], computing the saddlepoints $t_{n_i}^\star$ using the saddlepoint condition, and then calculating the updated $\{\boldsymbol{\xi}_{i+1}, A_{i+1}\}$ by inverting the closed system,

$$\sum_{k=1}^{K} \delta\xi_{k_i} (t_{n_i}^\star)^k + \delta A_i = S^{(n)} - \psi_K(t_{n_i}^\star; \boldsymbol{\xi}_i) - A_i, \quad \text{for } n = 1, 2, ..., K.$$ (35)

where,

$$\delta\boldsymbol{\xi}_i = \boldsymbol{\xi}_{i+1} - \boldsymbol{\xi}_i, \quad \delta A_i = A_{i+1} - A_i,$$ (36)

iterating this procedure until convergence is detected i.e. $\delta\boldsymbol{\xi}_i \to \boldsymbol{0}, \delta A_i \to 0$. To calculate the first layer $\{c_{k,0}\}$ we we use the expansion in Eq. (27) given that the second term on the r.h.s disappears when evaluated at the saddles points (due to the saddle point condition) and that the l.h.s is given by the first expression in Eq. (33) under the same evaluation. Thus we invert the matrix,

$$\left(\left. \frac{\mathrm{d}^2\psi_K}{\mathrm{d}t^2} \right|_{t_n^\star} \right)^{1/2} A_0^{(n)} = \sum_{k=0}^{K} c_{k,0}(\boldsymbol{x})(t_n^\star)^k.$$ (37)

From a computational perspective it is worth noting that $t_n^\star$, $\{\boldsymbol{\xi}, A\}$, and $\{c_{k,m}\}$ are all functions of position, and so this algorithm (Eqs. (35) to (37)) has to be repeated every time the receiver position changes. However, as we move position we can use the solutions $\{\boldsymbol{\xi}, A\}$ from a nearby point as initial guesses for the algorithm in a similar manner to the generation of ray bifurcation curves in Section II.B.2. These iterations and inversions may appear cumbersome but as post-processing corrections to the ray field there isn't a significant increase in computational burden.

---

[b] $K+1$ is the order of the polynomial ψ_K'.
[c] Even though we may only require these cases, it is still useful to prepare a method capable of $K > 2$ maps.
[d] For real receivers this promotes convergence.

American Institute of Aeronautics and Astronautics

IV. Application to an isothermal parallel-shear flow.

To the illustrate the method we have developed in this paper, we will consider an isothermal parallel shear flow such that $a = 1$, $\bar{\rho} = \text{const.}$, and $\boldsymbol{M} = \delta_{i1}\bar{u}/\bar{c}_\infty = \delta_{i1}M$. It is well known that Eqs. (1) can be manipulated into a single wave equation governing the acoustic density, and that this is the time harmonic solution to Lilley's equation for a point source,[26]

$$\mathscr{L}_\omega G_\omega = D_\omega\left(D_\omega^2 - \bar{c}_\infty^2\nabla^2\right)G_\omega + 2\bar{c}_\infty^2\nabla\bar{u}\cdot\nabla\frac{\partial}{\partial x}G_\omega = D_\omega\bar{c}_\infty^2\delta(\boldsymbol{x} - \boldsymbol{x}_s), \tag{38}$$

where G_ω is the Green's function, and $D_\omega = (-\mathrm{i}\omega + \bar{u}\,\partial/\partial x)$. Even though it is G_ω that matches with ρ' for a point source solution, we will express our results in terms of $\mathbb{G}_\omega$ which solves Eq. (38) with r.h.s equal to $\bar{c}_\infty^2\delta(\boldsymbol{x} - \boldsymbol{x}_s)$. The two are related via,

$$G_\omega = -\left(\mathrm{i}\omega + \bar{u}_s\frac{\partial}{\partial x_s}\right)\mathbb{G}_\omega. \tag{39}$$

In the above a Cartesian coordinate system $\{x, y, z\}$ has been chosen so that x is in line with the direction of flow, so the shear flow is a function of y, z only. In the following it is convenient to convert to a cylindrical coordinate system $\{x, r, \varphi\}$, giving $M = M(r)$ and $\boldsymbol{x}_s = (x_s, r_s\cos\varphi_s, r_s\sin\varphi_s)$, and further use spherical polars for the receiver position $\boldsymbol{x}_R = R(\cos\theta, \sin\theta\cos\varphi, \sin\theta\sin\varphi)$ as shown in Figure 4. The coordinates are related via,

$$R = \sqrt{x^2 + r^2}, \quad r = \sqrt{y^2 + z^2}, \quad \theta = \arccos\left(\frac{x}{R}\right), \quad \varphi = \arccos\left(\frac{y}{r}\right). \tag{40}$$

A. Modal solution.

A high-frequency far-field modal solution to Eq. (38) was constructed by Wundrow & Khavaran,[12] and this will serve as the benchmark for the ray-solution. It is given by,

$$\mathbb{G}_\omega \sim \frac{\mathrm{i}\,\mathscr{G}_\omega}{\bar{c}_\infty k_0(1 - M_s\cos\theta)^2}\sum_{n=-\infty}^{\infty}\left(\frac{2}{k_0}\frac{\sqrt{-\eta_n(r_s)}}{r_sQ_n(r_s)}\right)^{1/2}\text{Ai}(\eta_n(r_s))\mathrm{e}^{\mathrm{i}n\Delta\varphi + \mathrm{i}k_0(\zeta_n - R\sin^2\theta)}, \tag{41}$$

where $\mathscr{G}_\omega \equiv \mathrm{e}^{\mathrm{i}k_0R}/4\pi R$ is the Helmholtz Green's function and,

$$\eta_n(r) \equiv -\left(\frac{3}{2}k_0\zeta_n(r)\right)^{2/3}, \quad \zeta_n(r) \equiv \int_{r_\delta}^{r}Q_n(r)\,\mathrm{d}r, \quad Q_n^2(r_\delta) = 0, \tag{42}$$

$$rQ_n(r) \equiv \sqrt{r^2q^2 - (n/k_0)^2}, \quad q(r) \equiv \sqrt{(1 - M(r)\cos\theta)^2 - \cos^2\theta}. \tag{43}$$

There are a few of points worth mentioning that concern Eq. (41). Firstly, and most importantly, it contains some high-frequency apparatus itself and therefore would require benchmarking. This has been undertaken in Ref. 12 where it was shown that good agreement was reached against an exact numerical computation for Strouhal numbers as low as $1/2$. Secondly, the high-frequency modelling restricts the receiver ranges in θ such that $\mathrm{d}Q_n^2(r_\delta)/\mathrm{d}r \neq 0$, also known as a first order turning-point criterion. The presence of the Airy function is indicative of this requirement, providing uniformity in the modes when $r_s = r_\delta$, and is not an indication of a caustic in the 3D ray field as in Eq. (31). Lastly, this solution is also asymptotic in the sense that it is valid in the far-field i.e. $R \to \infty$, and ultimately independent of the x-coordinate due to translational invariance of the flow in x. Numerical realizations of Eq. (41) will reflect this if the source point satisfies $|\boldsymbol{x}_R| \gg |\boldsymbol{x}_s|$.
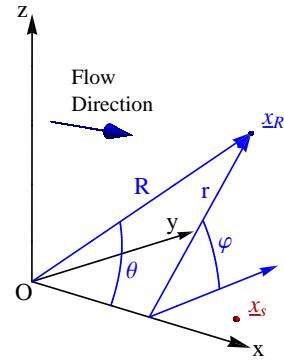
Figure 4. Coordinate system used to specify flow regime and receiver position.
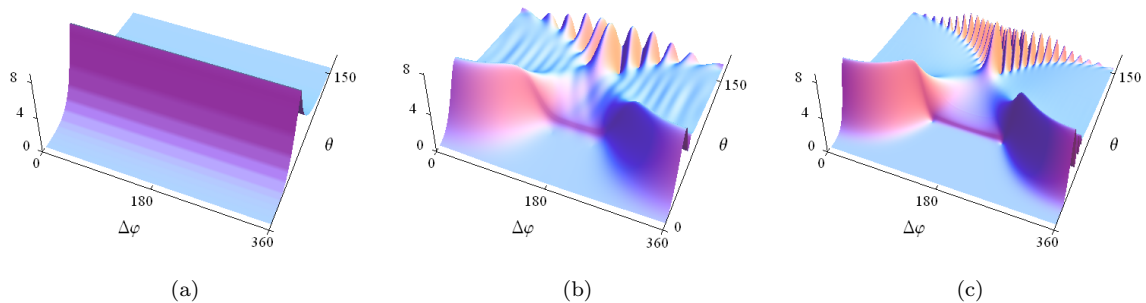
Figure 5. Example fields produced by Eq. (41). Plots show $10^4 \times |\mathbb{G}_\omega/\mathscr{G}_\omega|$ for **a)** $x_s = 0$, $r_s = 0$, $St = 2$; **b)** $x_s = 0$, $r_s = 0.75$, $St = 2$; **c)** $x_s = 0$, $r_s = 0.75$, $St = 5$.

As an example of the fields we can expect from Eq. (41), Figure 5 shows $10^4 \times |\mathbb{G}_\omega/\mathscr{G}_\omega|$ computed with $R = 200$, for both an on-axis $(x_s = 0, r_s = 0, \varphi_s = 90°)$[e] and off-axis "shear-layer" $(x_s = 0, r_s = 0.75, \varphi_s = 90°)$ source for Strouhal numbers $St = 2$ and 5. Here we have used the Strouhal number $St = k_0 r_J/\pi M_J$, with $r_J = 1/2$ the effective jet radius, $M_J = 0.9$ the jet centerline Mach no., and flow profile $M(r) = M_J \text{sech}^2(2r)$. This gives wavenumbers of $k_0 = 11.3$ and $k_0 = 28.27$ for $St = 2, 5$ respectively. Note that first order turning-point assumption has limited the calculation to $\theta \le 150°$, and that the fields are expressed in terms of the asymmetry variable $\Delta\varphi = \varphi - \varphi_s$, $0 \le \Delta\varphi \le 360°$, since for the same r_s, different φ_s fields are simply translations of each other in φ. It should be clear from Eq. (41) and Figure 4 that both φ and $\Delta\varphi$ have a period equal to $360°$.

It may appear that we have chosen to compute $\mathbb{G}_\omega/\mathscr{G}_\omega$ rather than $\mathbb{G}_\omega$ for numerical reasons, however the former is more significant than the latter as a measure of flow-interaction. It describes the change in acoustic field directivity due to the presence of a flow as opposed to a field without it. It is clear from these plots that the off-axis source solution contains a richer flow-interaction structure - its interference patterns are enough to demonstrate this - and coupled with the fact that $r_s \ne 0$ is more representative of high-frequency jet noise sources, qualifies it for further analysis here.

B. Results

1. Ray calculations.

Ray calculations are made using the theory contained in Section II. Using the same flow profile and off-axis source position used to calculate the modal solution in Figure 5, we set the observer variable α of Section 2 to the spherical polar angle θ, keeping $\Delta\varphi$ constant. Varying θ in this way generates cross sections of the Green's function shown in Figure 5. To illustrate typical ray solutions that we encounter under this parameterization, Figures 6(a) and 6(b) show $\Re(\boldsymbol{x}(\tau))$ trajectories for a receiver curve in the forward arc, $\theta < 90°$, $\Delta\varphi = 300°$, and in the rear arc, $101° < \theta < 150°$, $\Delta\varphi = 180°$, with a receiver radius $R = 7$.

In Figure 6(a) there exists a multiplicity of real solutions as both rays that propagate directly towards the receiver and rays that are refracted indirectly, i.e. a bent towards the receiver by the flow, reach the same points. As θ is increased this region of real multiplicities terminates as the flow cannot continue to refract these rays upwards indefinitely, and instead they propagate into regions for which $z < 0$. If θ is decreased these two rays coalesce at a caustic and continuation across the caustic produces one physical complex ray (shown in red). Locally, this behavior is governed by the fold bifurcation, as demonstrated in Figure 6(c) using the bifurcation curve Γ_λ for the ray parameter, λ. To incorporate the complex branches we have shown $\Gamma_\lambda(\theta)$ when $\Gamma_\lambda \in \mathbb{R}$, and $\Re(\Gamma_\lambda(\theta)) + \Im(\Gamma_\lambda(\theta))$ when $\Gamma_\lambda \in \mathbb{C}$. The colors of the bifurcation curves correspond to the rays shown in Figure 6(a), where the black branch is excluded on physical grounds.

---

[e]Taking appropriate limits in Eq. (41) for $r_s \to 0$.
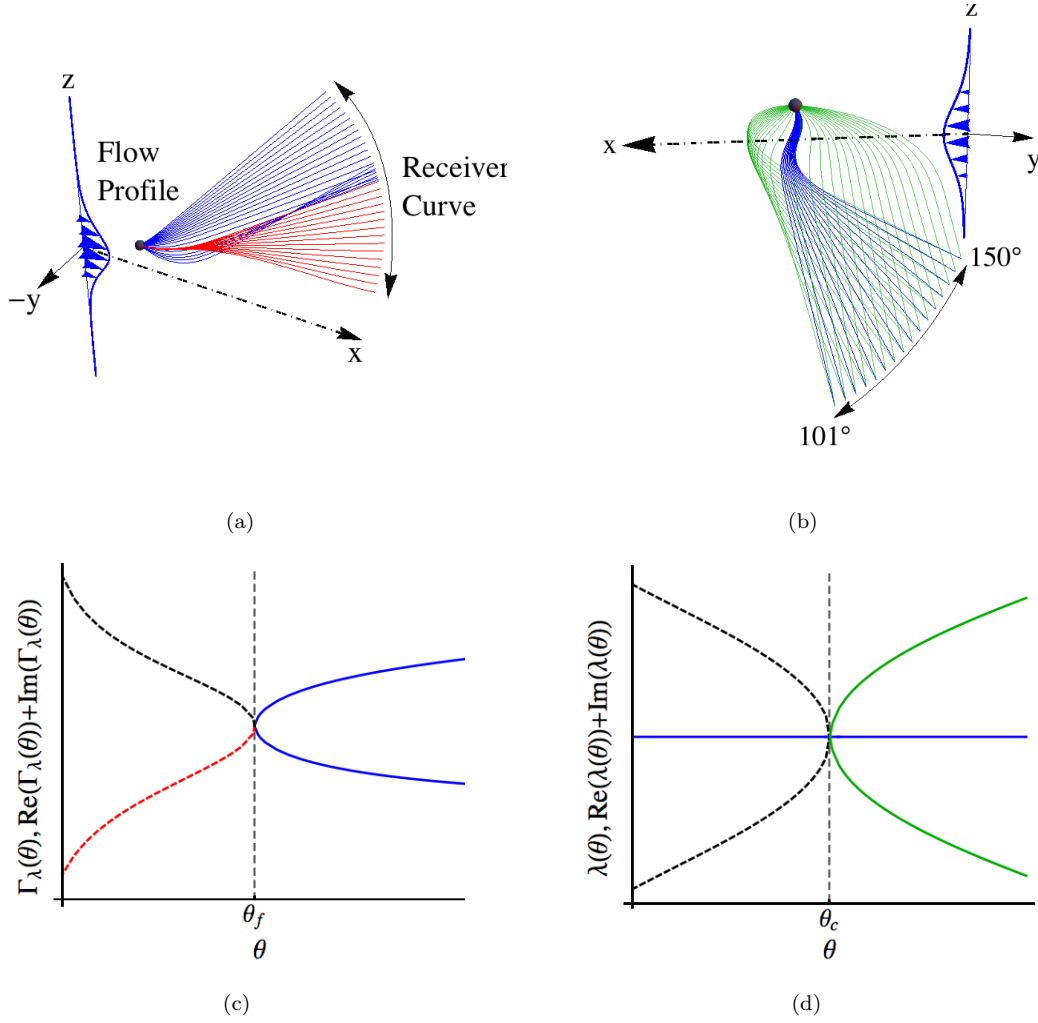
Figure 6. Real part ray trajectories $\Re(\boldsymbol{x}(\tau))$ (a,b), and bifurcation curves (c,d). Rays: (a) receiver curve $\Delta\varphi = 300°$, $R = 7$, blue - real rays, red - complex rays; (b) a triplet of real rays reaching $\Delta\varphi = 180°$, $R = 7$, red rays leave the $\Delta\varphi = 180°$ plane. Bifurcation curves, solid lines Γ_λ, dashed $\Re(\Gamma_\lambda) + \Im(\Gamma_\lambda)$: (c) fold bifurcation, θ_f, solid blue line - real rays, dashed red - physical complex ray, dashed black - unphysical complex ray; (d) cusp bifurcation, θ_f, solid blue/green - real ray contributions, dashed black - no contribution.

The second ray trajectory plot shown in Figure 6(b) has a receiver curve located directly underneath the source w.r.t the jet axis. Here, a triplet of real rays reach the receiver curve where two of the contributions (shown in green), both physical and carrying the same numeric contribution to the field, propagate outside of the $\Delta\varphi = 180°$ plane. The interference and coalescence of a 3 ray system generates a cusp caustic, which upon its symmetry line (such as that shown in Figure 6(b)) is governed by a pitchfork bifurcation as shown in Figure 6(d), again using Γ_λ. The triplet of real rays in Figure 6(b) correspond to the color-coded branches for $\theta \geq \theta_c$ in Figure 6(d), where $\theta_c \approx 101°$ in Figure 6(b). For $\theta < \theta_c$ only one contribution is made to the ray field, though this is not shown in the Figure 6(b) in order to distinguish between the coalescing triplet.

The ray trajectories we have shown in Figure 6 suggest that there is more than one caustic structure in the off-axis Green's function. Although these multiplicities and caustics pertain to $R = 7$, they still persist in the far-field evaluation $R = 200$, albeit with different fold and cusp positions in $\theta, \Delta\varphi$-space. To aid the following discussion of ray computations, Figure 7 shows Figure 5(c) as a 2D directivity map overlaid by caustic structures for $R = 200$. This figure shows the existence of a fold caustic θ_f, and cusp caustic θ_c (notably extending beyond the range of the modal solution), both of which are symmetric about the line $\Delta\varphi = 180°$, and are functions of $\Delta\varphi$ so that $\theta_{c,f} = \theta_{c,f}(\Delta\varphi) = \theta_{c,f}(360° - \Delta\varphi)$. Figure 7 also shows a
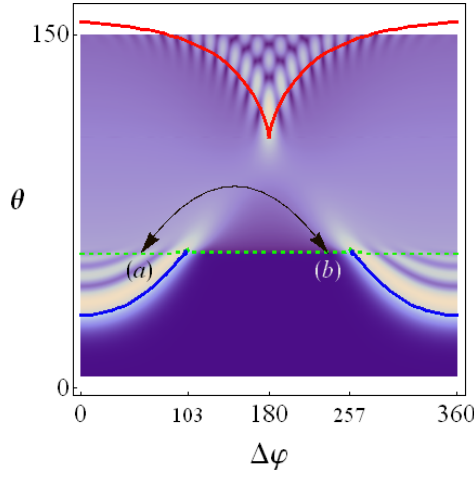
Figure 7. The caustic structures found in the ray solution of Eq. (41) for $x_s = 0$, $r_s = 0.75$, $\varphi_s = 90°$, $R = 200$, $St = 5$. **Blue solid line, fold caustic, θ_f; red solid line, cusp caustic, θ_c; green dashed line, non-canonical structure, θ_d.**

non-canonical feature, θ_d, mapped out by the green dashed line. Its union, between $\Delta\varphi \approx \{103°, 257°\}$, with θ_f delineates a region exclusive to complex rays known as the cone of silence. This region exists for low angles θ, and is shaded dark blue in Figure 7.

The effect of these caustics on the magnitude of the ray solution can be seen in Figure 8, where cross sections of $|\mathbb{G}_\omega/\mathscr{G}_\omega|$ have been plotted against the modal solution for $\Delta\varphi = \{0°, 60°, 150°, 180°\}$ with $St = 5$. Where necessary the plot range is extended to $160°$ to include all singularities due to the cusp.

As expected the ray solution provides excellent agreement with the modal solution for all cross sections except in the region of these caustics where the divergence is marked. A particularly satisfactory aspect of the ray solution is that within the cone of silence the exponentially decaying behavior is captured well, indicating the success of the natural parameter continuation (Section II.B) at tracking complex branches.

Before we discuss the corrections to the divergences, it is worth addressing the features of the ray solution that pertain to the non-canonical points θ_d, as this structure will have a say on how we apply the uniform solutions. Physically, the crossing of θ_d can be explained in relation to the effectiveness of the flow-profile at refracting indirect rays to the observer, just as in Figure 6(a). For example, at point (a) in Figure 7 (corresponding to $\Delta\varphi = 60°$) an increase of θ sees the loss of an indirect ray, that instead of being refracted to the receiver, propagates away from the receiver curve to make a contribution at $\Delta\varphi + 180°$ (shown as point (b) in Figure 7), directly on the opposite side of the jet (w.r.t jet axis) from the receiver curve. For $\Delta\varphi < 103°$, $\Delta\varphi > 257°$ this disappearance limits the interference we see in the vicinity of the fold and thus explains the restricted oscillation between θ_f and θ_d in Figures 8(a) and 8(b).

The change in the number of real rays (i.e. not in multiples of 2) crossing θ_d seemingly contravenes the conservation of rays that we have relied upon up until now. This will limit the range of θ to which we can apply the diffraction catastrophes in Section III, as the number of rays, and thus roots, must be conserved in order to apply Ψ_K.

A further consequence of this non-canonic structure is that it delineates part of the cone of silence, namely $103° < \Delta\varphi < 257°$ without singularity. This is unusual for two reasons: first, the fold that delineates the cone of silence for $\Delta\varphi < 103°$, $\Delta\varphi > 257°$ appears to terminate in real space and; secondly, the transition into the cone of silence has no bifurcation and therefore rays cannot be continued into the cone of silence using the methods of Section II.B.2. For instance, continuing the point (b) in Figure 7 into the cone silence sees the real ray contribution terminate with a finite amplitude; rotation about θ_d into the cone of silence leads to rapid divergence of the Newton method Eq. (21). Hence the required complex ray to compute field must be continued from a $\Delta\varphi$ position for which the cone of silence is delineated by a fold caustic.

From a qualitative point of view the absence of a singularity when crossing θ_d into the cone of silence, e.g. Figure 8(c), makes for interesting comparison with a field where θ crosses a fold, e.g. Figure 8(a), as the amplitude of the former is significantly smaller. Clearly, the explanation for this lies in the significant rise in amplitude of a field near a caustic.

American Institute of Aeronautics and Astronautics
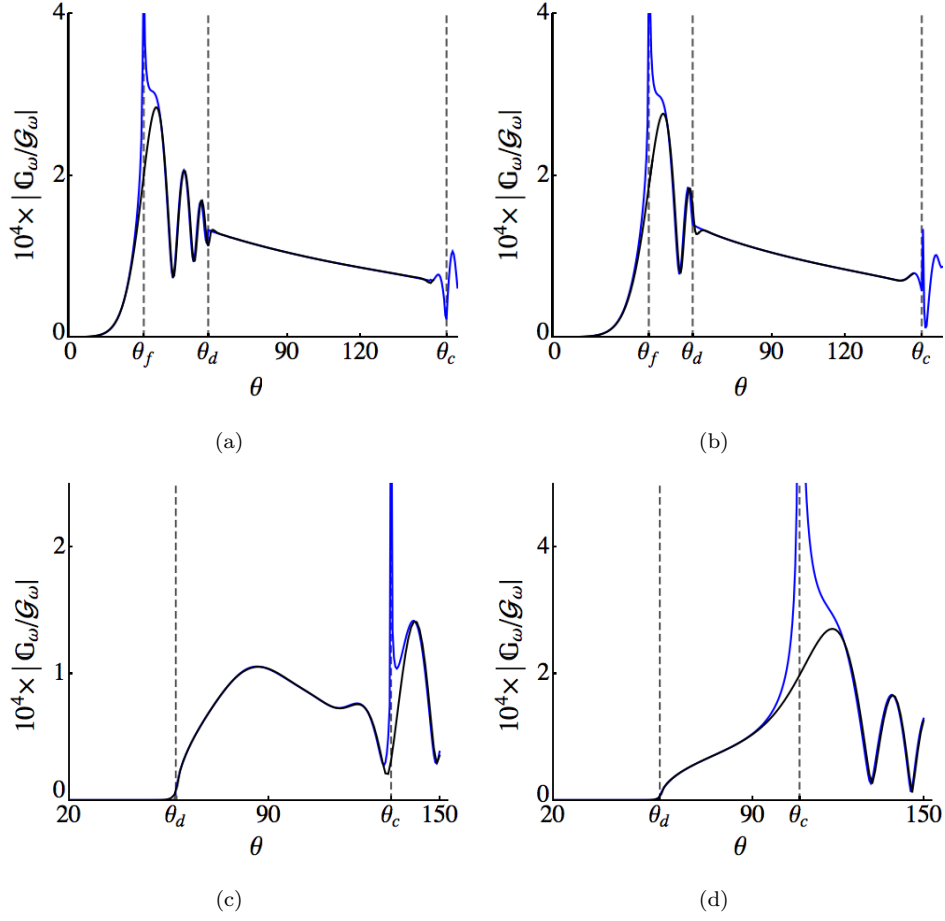
Figure 8. $10^4 \times |\mathbb{G}_\omega/\mathscr{G}_\omega|$ **cross sections for** $\Delta\varphi = \text{const.}$ **with** $x_s = 0$, $r_s = 0.75$, $St = 5$. **Non-canonic point,** θ_d; **fold caustic,** θ_f; **cusp caustic,** θ_c. **Black lines, modal solution; blue lines, ray solution.** (a) $\Delta\varphi = 0°$; (b) $\Delta\varphi = 60°$; (c) $\Delta\varphi = 150°$; (d) $\Delta\varphi = 180°$.

2. Uniform calculations.

To correct the divergences shown in Figure 8 we apply the machinery of Section III. Given that θ_d doesn't engender an amplitude singularity, all singularities in this problem are governed by the cuspoids. In particular only the fold and cusp caustics governed by Ψ_1 and Ψ_2, respectively, are required. Using only the $m = 0$ layer in Eq. (31) we compute uniform solutions using one term $k = 0$, and two term $k = 0, 1$ expansions. For the special case $\Delta\varphi = 180°$, $c_{1,0} = 0$, $\forall\theta$, and so a two term expansion uses $k = 0, 2$. Figure 9 shows the amplitude and phase of the uniform expansions against the modal solution for the cross sections $\Delta\varphi = \{0°, 150°, 180°\}$. In the cases where θ_d limits application of the uniform asymptotics due to its non-canonical nature, we have either reverted to the ray expansion (away from $\theta_{c,f}$) or decreased the plot range.

It is clear that the amplitudes in Figure 9 show a great improvement in the region of the caustics where the divergence is almost completely corrected. Perhaps the worst case is shown in Figure 9(a) where the first term expansion erroneously predicts zeros on the oscillatory side of the fold caustic θ_f. The other notable disparity is shown in Figure 9(e) where a small jump at θ_c is the product of the numerics coping with the integrable singularity mentioned in Section III. In general as θ moves away from the caustic we see that a one term expansion becomes less effective at matching the modal solution. The two term expansion on the other hand maintains an excellent approximation. The reason the two term is superior to the one term expansion as the receiver moves increasingly away from the caustic can be understood by expanding Ψ_K and its derivatives (those that appear in Eq. (31)) to leading order about all of the n_K contributing saddles

(a)

(b)

(c)

(d)

(e)

(f)
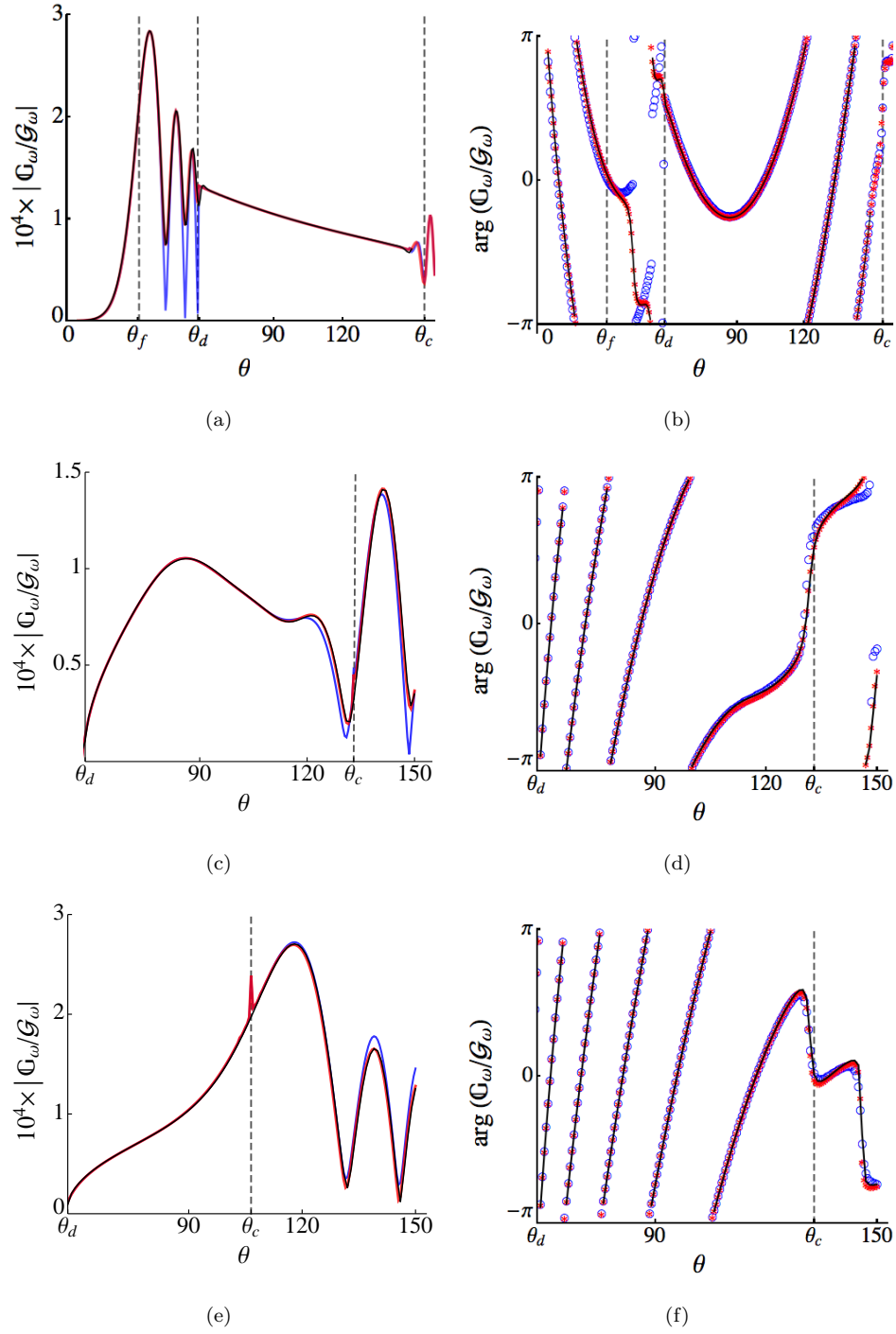
Figure 9. Uniform asymptotic solutions. (a, c, e) pertain to $10^4 \times |\mathbb{G}_\omega/\mathcal{G}_\omega|$, black line - modal solution, blue line - one term exp., red line - two term exp. (b, d, f) pertain to $\arg(\mathbb{G}_\omega/\mathcal{G}_\omega)$, black line - modal solution, blue $\circ$ - one term exp., red $*$ - two term exp. $\theta_{c,f,d}$ as in Figure 8. (a,b) $\Delta\varphi = 0°$; (c,d) $\Delta\varphi = 150°$; (e,f) $\Delta\varphi = 180°$.

American Institute of Aeronautics and Astronautics

using the saddle-point technique (using notation of Section III). Doing so we have,

$$\Psi_K(\tilde{\boldsymbol{\xi}}) \sim \sum_{n=1}^{n_K} \left(\frac{2\pi i}{k_0 \psi_K''(t_n^\star)}\right)^{1/2} e^{ik_0\psi_K(t_n^\star)}, \quad e^{-i\pi/2} k_0^{\frac{k+1}{K+2}} \frac{\partial \Psi_K(\tilde{\boldsymbol{\xi}})}{\partial \tilde{\xi}_k} \sim \sum_{n=1}^{n_K} \left(\frac{2\pi i}{k_0 \psi_K''(t_n^\star)}\right)^{1/2} (t_n^\star)^k e^{ik_0\psi_K(t_n^\star)}, \quad (44)$$

where $'' \equiv \mathrm{d}^2/\mathrm{d}t^2$. Substitution into Eq. (31), taking only the $m = 0$ layer, and collecting all $t_n^\star$ terms together we have,

$$I \sim \sum_{n=1}^{n_K} \underbrace{\sum_{k=0}^{K} c_{k,0} \left(\psi_K''(t_n^\star)\right)^{-1/2} (t_n^\star)^k e^{ik_0(\psi_K(t_n^\star)+A)}}_{A_0^{(n)} e^{ik_0 S^{(n)}}}, \quad (45)$$

which is in fact just another statement of the matrix system given in Eq. (37). Equation (45) demonstrates that far off caustic we need to incorporate more than just the $k = 0$ term (proportional to Ψ_K) to match up with the ray field. Only in the region close to the caustic will the $k = 0$ term make a good approximation on its own. As θ moves closer to the caustic the coalescing saddle points $t_n^\star$ tend to zero, since if we have chosen the correct ψ_K, then at a caustic they are roots of $\psi_K'(t_n^\star; \mathbf{0})$. This allows us to neglect the $k > 0$ terms in Eq. (45) without diminishing accuracy.

So far we have made little mention of the phase computations. The phase of the ray field at caustics does not diverge away infinitely from the true field in the way the amplitude does, in fact the phase propagated along the ray has an integrable singularity at the caustic,[16] which at most, manifests itself as a jump. If we are interested in the phase we do not need to recourse to uniform computations, however we have done this to further compare the one and two term expansions. Analyzing Figure (9) we reach a similar conclusion to that of the uniform amplitude: the two term expansion provides a better match, than the one term, though the difference is not considerable overall. The only major disparity is as before i.e. in the vicinity of the fold (θ_f in Figure 9(b)). Here Ψ_1 is not adequate for calculating the field, the zeros predicted using this function alone leads to several jumps in the phase.

V. Conclusion

In this paper we have developed a complex ray-tracing tool for calculating high-frequency acoustic fields in arbitrary homentropic mean flows due to a point source. Three of the most common problems that arise in the application of ray theory: multiplicity of solutions, amplitude singularities at caustics and determination of complex rays, have been tackled. Multiple solutions were found by formulating a ray boundary value problem (BVP) that represented the receiver point explicitly, which in turn allowed us to define an equivalent iterative system using a multi-dimensional Newton method. Supported by the implicit function theorem we generated branches of solutions in the ray parameters via natural parameter continuation in receiver space. We then used the concept of structural stability to analytically continue these branches around caustics, with the dual intension of finding complex branches (when they existed) and maximizing our ability to identify an appropriate diffraction catastrophe to correct the amplitude singularities at caustics. After developing the basis of our ray tool, we applied it to an isothermal parallel shear flow problem whose acoustic propagation is governed by Lilley's equation; the first numerical realization of complex rays using ray-tracing for this problem. Apart from the expected amplitude singularities engendered by the presence of a fold and cusp caustic, the complex ray method showed good agreement with a modal solution, particularly in the cone of silence. In the locality of these caustics a two term diffraction catastrophe expansion proved effective at correcting the divergence, matching with the ray solution off-caustic. A combined effort of two term expansion and ray solution provided excellent agreement in both amplitude and phase globally. We also noted a non-canonical feature of the ray field related to the shear layer's refractive properties. As a mathematical phenomena this disappearance - which apparently contravenes the conservation of rays - is unresolved: however, it does not undermine our method as a numerical tool. The results shown in this paper have altogether proved encouraging and it is the conclusion of this paper that application of the ray tool to more complicated flows than the one considered here would meet with similar success.

American Institute of Aeronautics and Astronautics

References

[1] Lighthill, M. J., "On sound generated aerodynamically. I. General theory," *Proceedings of the Royal Society of London. Series A. Mathematical and Physical Sciences*, Vol. 211, No. 1107, 1952, pp. 564–587.

[2] Lighthill, M. J., "On sound generated aerodynamically. II. Turbulence as a source of sound," *Proceedings of the Royal Society of London. Series A. Mathematical and Physical Sciences*, Vol. 222, No. 1148, 1954, pp. 1–32.

[3] Lilley, G. M., "On the noise from jets," *Agard cp-131*, 1974, pp. 13–1.

[4] Goldstein, M. E., "A generalized acoustic analogy," *Journal of Fluid Mechanics*, Vol. 488, 2003, pp. 315–333.

[5] Brekhovskikh, L., *Waves in Layered Media 2e*, Vol. 16, Elsevier, 2012.

[6] Candel, S. M., "Numerical solution of conservation equations arising in linear wave theory: application to aeroacoustics," *Journal of Fluid Mechanics*, Vol. 83, 1977, pp. 465–493.

[7] Freund, J. and Fleischman, T., "Ray traces through unsteady jet turbulence," *International Journal of Aeroacoustics*, Vol. 1, No. 1, 2002, pp. 83–96.

[8] Avila, G. S. S. and Keller, J. B., "The high-frequency asymptotic field of a point source in an inhomogeneous medium," *Communications on Pure and Applied mathematics*, Vol. 16, No. 4, 1963, pp. 363–381.

[9] Durbin, P. A., "High frequency Green function for aerodynamic noise moving media, Part I: general theory," *Journal of Sound and Vibration*, Vol. 91, 1983, pp. 519–525.

[10] Gilmore, R., *Catatrophe theory for scientists and engineers*, Courier Dover Publications, 1993.

[11] Ludwig, D., "Uniform asymptotic expansions at a caustic," *Communications on Pure and Applied Mathematics*, Vol. 19, No. 2, 1966, pp. 215–250.

[12] Wundrow, D. W. and Khavaran, A., "On the applicability of high-frequency approximations to Lilley's equation," *Journal of sound and vibration*, Vol. 272, No. 3, 2004, pp. 793–830.

[13] Van Dyke, M., *Perturbation methods in fluid mechanics*, Vol. 28, Parabolic Press Stanford, 1975.

[14] Bleistein, N., *Mathematical methods for wave phenomena*, Academic Press, 1984.

[15] Whitham, G. B., *Linear and nonlinear waves*, Vol. 42, John Wiley & Sons, 2011.

[16] Hayes, W. D., "Kinematic wave theory," *Proceedings of the Royal Society of London. A. Mathematical and Physical Sciences*, Vol. 320, No. 1541, 1970, pp. 209–226.

[17] Egorchenkov, R. A. and Kravtsov, Y. A., "Complex ray-tracing algorithms with application to optical problems," *JOSA A*, Vol. 18, No. 3, 2001, pp. 650–656.

[18] Sambridge, M. S. and Kennett, B. L. N., "Boundary value ray tracing in a heterogeneous medium: a simple and versatile algorithm," *International Journal of Geophysics*, Vol. 101, 1990, pp. 157–168.

[19] Keller, H. B., *Numerical methods for two-point boundary-value problems*, Dover Publications New York, NY, 1992.

[20] Berry, M. V. and Upstill, C., "Catastrophe optics: morphologies of caustics and their diffraction patterns," *Prog. Opt*, Vol. 18, 1980, pp. 257–346.

[21] Thomson, C. J. and Chapman, C. H., "An introduction to Maslov's asymptotic method," *Geophysical Journal International*, Vol. 83, No. 1, 1985, pp. 143–168.

[22] Berry, M. V. and Howls, C. J., "Integrals with coalescing saddles," *Digital Library of Mathematical Functions, http://dlmf.nist.gov*, 2006.

[23] Bleistein, N. and Handelsman, R. A., *Asymptotic Expansions of Integrals*, Dover, 1986.

[24] Hanyga, A., "Canonical functions of asymptotic diffraction theory associated with symplectic singularities," *Banach Center Publications*, Vol. 39, 1997, pp. 57–71.

[25] Connor, J. and Curtis, P., "Differential equations for the cuspoid canonical integrals," *Journal of Mathematical Physics*, Vol. 25(10), 1984, pp. 2895–2902.

[26] Goldstein, M. E., "Aeroacoustics," *New York, McGraw-Hill International Book Co., 1976. 305 p.*, Vol. 1, 1976.